



A symmetrical CO₂ peak and asymmetrical climate change during the middle Miocene

Shunchuan Ji^{a,b}, Junsheng Nie^{a,*}, Alex Lechler^c, Katharine W. Huntington^d,
Emma O. Heitmann^e, Daniel O. Breecker^e

^a Key Laboratory of Western China's Environmental System (Ministry of Education), College of Earth and Environmental Sciences, Lanzhou University, Lanzhou 730000, China

^b State Key Laboratory of Loess and Quaternary Geology, Institute of Earth Environment, Chinese Academy of Sciences, Xi'an 710075, China

^c Department of Geosciences, Pacific Lutheran University, Tacoma, WA 98447, USA

^d Department of Earth and Space Sciences, University of Washington, Seattle, WA 98195-1310, USA

^e Department of Geological Sciences, University of Texas at Austin, Austin, TX 787131, USA



ARTICLE INFO

Article history:

Received 21 November 2017

Received in revised form 6 July 2018

Accepted 8 July 2018

Available online 30 July 2018

Editor: D. Vance

Keywords:

Miocene
atmospheric CO₂
uncertainty
paleosols
China

ABSTRACT

Understanding the future trajectory of Earth's climate requires knowledge of shifts in atmospheric CO₂ concentrations during past warm episodes. The Miocene Climatic Optimum (MCO, ~17–14 Ma) was likely the warmest episode of the past 25 Myr, and thus atmospheric CO₂ concentrations during this interval are of particular interest. However, CO₂ records across the middle Miocene are rather scattered and data are notably sparse for the latter part of the MCO. Here we present a paleosol-based CO₂ record from the Tianshui Basin, northern China, spanning 17–7 Ma. Our results show elevated mean CO₂ during the second half of the MCO corresponding with some of the lowest benthic $\delta^{18}\text{O}$ values and highest benthic $\delta^{13}\text{C}$ values, as part of the “Monterey excursion”, published for the Neogene. This result supports the idea that the broader Monterey excursion was primarily associated with a CO₂ maximum, not carbon burial and CO₂ minima as previously interpreted. The new CO₂ record, along with previous CO₂ records based on paleosols, stomata and foraminiferal boron isotope compositions, also suggests that mean CO₂ across the MCO was elevated compared with the immediately following (post-MCO, 14–11 Ma, >80% probability) and immediately preceding (pre-MCO, 20–17 Ma, 70% probability) time periods. The most probable magnitude of the MCO CO₂ peak is 20% higher than post-MCO and 12.5% higher than pre-MCO levels. Larger factors, of perhaps 50% higher CO₂, likely apply in narrower (<1 Myr) time slices. CO₂ records from each proxy individually support the conclusion of modestly elevated MCO CO₂, although large temporal gaps exist in records from any one proxy. Using all proxies together, we estimate average MCO CO₂ of 375+150/–100 (84th and 16th percentile) ppm. Although mean MCO CO₂ was elevated, the MCO was also characterized by highly variable CO₂. In addition, determinations from all three proxies suggest that at times during the MCO, CO₂ levels were as low as they were following the ice sheet expansion of the Miocene Climate Transition. Furthermore, pre-MCO CO₂ levels are indistinguishable from post-MCO CO₂ levels (60% probability of pre-MCO CO₂ > post-MCO CO₂), despite significantly lower benthic $\delta^{18}\text{O}$ values during the former. We conclude that 1) the MCO was a period of slightly elevated and highly variable CO₂ compared with the immediately preceding and following intervals, and 2) neither CO₂ decrease, orbitally-controlled seasonality over Antarctica nor the confluence of these factors was sufficient to cause Miocene Climate Transition ice sheet expansion. Rather strengthening of the Antarctic Circumpolar Current and Southern Ocean cooling related to closure of the eastern Tethys was a necessary first step.

© 2018 Elsevier B.V. All rights reserved.

1. Introduction

Atmospheric CO₂ levels have increased from ~280 ppm during the late Holocene preindustrial period to above 400 ppm

* Corresponding author.

E-mail address: jnie@lzu.edu.cn (J. Nie).

(Dlugokencky and Tans, 2016) and are projected to go higher (Meinshausen et al., 2011). The current atmospheric CO₂ level exceeds the maximum Pleistocene CO₂ levels measured in ice cores (Bereiter et al., 2015) and is roughly similar to those (Kürschner et al., 2008; Greenop et al., 2014) during the Miocene Climatic Optimum (MCO, 17.4–14 Ma, Mudelsee et al., 2014). The MCO is therefore a compelling interval to test our understanding of cli-

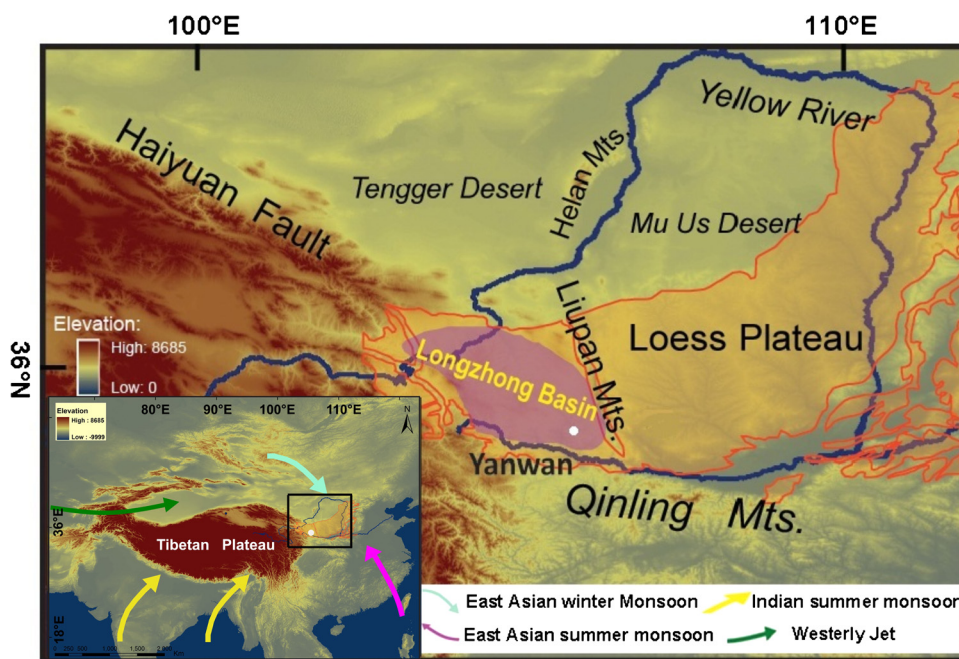


Fig. 1. Map showing the study site in the Tianshui Basin (the Yanwan section, marked by the white dot) on the Chinese Loess Plateau (orange area). (For interpretation of the colors in the figure(s), the reader is referred to the web version of this article.)

mate change and has been targeted for atmospheric $p\text{CO}_2$ research (e.g., Kürschner et al., 2008; Foster et al., 2012; Badger et al., 2013; Greenop et al., 2014).

Climate models do not reproduce the climate of the MCO using available proxy-based CO_2 estimates. To maintain warmth consistent with MCO proxy data, model simulations suggested the required CO_2 concentration is 800 ppm or above (Goldner et al., 2014). These CO_2 levels are higher than most proxy-based CO_2 determinations reported in the literature (e.g., Kürschner et al., 2008; Greenop et al., 2014). This data-model mismatch requires testing of existing proxy-based CO_2 records and consideration of other processes that might contribute to MCO warmth.

The MCO is recognized by a negative excursion in the $\delta^{18}\text{O}$ values of benthic foraminifera that temporarily interrupts the longer term trend of increasing benthic $\delta^{18}\text{O}$ values extending from Eocene to present (Zachos et al., 2008). The MCO is a distinctly asymmetric excursion beginning with a smaller magnitude (-0.2 to -0.4‰) ramp at its onset, centered at 17.4 Ma, and ending with a larger magnitude (0.9‰) ramp known as the Miocene Climate Transition (MCT) centered at 14 Ma (Mudelsee et al., 2014). The MCT is recognized as one of the major cooling steps of the Cenozoic (e.g., Flower and Kennett, 1994). The intervening 3.4 Myr constitutes the MCO, characterized by the lowest benthic $\delta^{18}\text{O}$ values of the Neogene (Zachos et al., 2008) and a global mean annual temperature $7.6 \pm 2.3^\circ\text{C}$ warmer than preindustrial.

A 4 Myr positive excursion in benthic $\delta^{13}\text{C}$ values, superimposed with eccentricity-paced $\delta^{13}\text{C}$ fluctuations (Holbourn et al., 2007), referred to as the Monterey Carbon Isotope Excursion (Vincent and Burger, 1985), largely coincides with, but clearly ends after, the benthic $\delta^{18}\text{O}$ minimum (Zachos et al., 2008) suggesting the occurrence of coupled carbon cycle–climate perturbations during the middle Miocene (Flower and Kennett, 1993). The Monterey Carbon Isotope Excursion was originally interpreted to record organic carbon burial and thus drawdown of CO_2 and associated cooling (Vincent and Burger, 1985). However, evidence for warming during the excursion (e.g., Miller et al., 1987) contradicted this interpretation. In addition, early records showed low and invariant atmospheric CO_2 concentrations across the Miocene (Pagani et al., 1999), further complicating interpretation of the Monter-

rey excursion. More recent CO_2 records show elevated CO_2 during part of the Monterey excursion (Kürschner et al., 2008; Foster et al., 2012), lending support to the idea that carbon emitted to the atmosphere as a result of the contemporaneous Columbia River volcanism/magmatism supported MCO warmth (e.g. McKay et al., 2014).

Cooling and polar ice sheet expansion across the MCT has been attributed to a decrease in CO_2 (Vincent and Burger, 1985; Foster et al., 2012; Holbourn et al., 2014), to orbitally-controlled decrease in seasonality over Antarctica (Holbourn et al., 2005, 2007) and to thermal isolation of Antarctica resulting from closure of the eastern Tethys and strengthened circumpolar circulation (Woodruff and Savin, 1989; Flower and Kennett, 1994; Shevenell et al., 2004). In this paper, we report a paleosol-based CO_2 record that augments late MCO CO_2 records and allows us to present a comprehensive, multiproxy perspective on climate- CO_2 relationships preceding, during, and immediately following the warmest global interval since the Eocene.

2. Material and methods

2.1. Setting and samples

Carbonate nodules were sampled from the paleosols preserved in the fluvio-lacustrine depositional sequences of the Yanwan section ($34^\circ58'\text{N}$, $105^\circ34'\text{E}$) in the north of the Tianshui Basin, Gansu, China (Zhang et al., 2013a) (Fig. 1). The Tianshui Basin is the southeast sub-basin of the Longzhong Basin, which is bounded by the Huajia Ling Mountain to the north, the Liupan Mountains to the east and northeast, and the western Qinlin Mountain to the south.

The Neogene strata in Yanwan section are ~ 280 m thick. The sedimentary environment of Yanwan's Neogene strata can be divided into three units (Fig. S1), from bottom to top, Unit 1 is from 280 to 148 m; Unit 2 is from 148 to ~ 20 m; Unit 3 is the uppermost ~ 20 m (Zhang et al., 2013a). The sedimentary environments of Units 1, 2, and 3 correspond to flood plains/distal fans, lake mudflats with sheet-floods, and flood plains, respectively (Fig. S1). The Yanwan section was dated by magnetostratigraphy to extend from 17.1 to 6.1 Ma (Zhang et al., 2013a). Coupled with

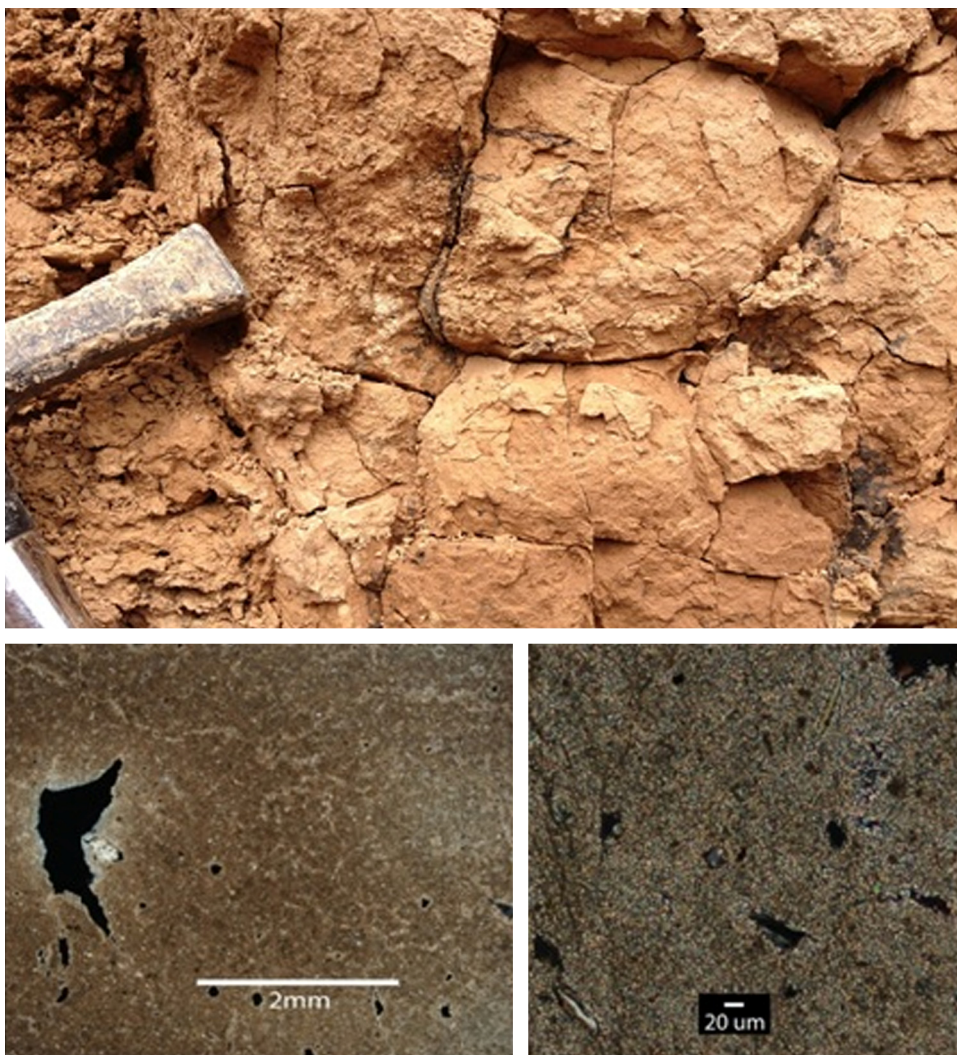


Fig. 2. Photograph of paleosol in the Tianshui Basin showing typical subangular blocky structure and carbonaceous root traces (top panel) and photomicrographs of a typical carbonate nodule in thin section (bottom panels), showing that the carbonate samples consist almost entirely of micrite.

magnetostratigraphy, two mammal fossils layers in the interval of ~10–6.5 Ma have been identified, with typical *Hipparion* fauna (Vallesian–Turolian) of the late Miocene (Zhang et al., 2013a). The sedimentation rates in the Yanwan section remain stable during the Miocene (Zhang et al., 2013a), and we therefore calculated the age of each stratigraphic level at which carbonate nodules were sampled by linear interpolation. The actual age of the formation of the soil carbonates is younger than the depositional age of the sediment in which they form. We sampled carbonates which formed >20 cm (typically 20 to 80 cm) below the paleosurface. Thus the carbonates started forming at the age of the stratigraphic level 20 to 80 cm higher than the level at which they were sampled. Soil carbonate nodules accumulate for thousands of years. We thus conservatively assign error bars on age by assigning the oldest possible age as the age of the stratigraphic layer in which the samples were collected and the youngest possible age as 10,000 yr younger than the age of the stratigraphic layer at the top of the relevant paleosol. This results in an average age error approximated by a uniform distribution within the window ± 0.01 Ma.

Paleosols were recognized in the field by soil structure and, in most of the paleosols sampled, well preserved root traces (Fig. 2; Retallack, 1988). Soil structure was typically subangular blocky, with peds 3–10 cm on a side (Fig. 2). Carbonaceous material defined the exterior of root traces, which varied in diameter from 1 mm to 1 cm (Fig. 2) and which were typically infilled with

silt. These coarse root traces were observed continuously from 130 down to 240 m (Fig. S1). Discrete paleosols were primarily recognizable by soil Bk horizons which tended to have abrupt, planar upper boundaries and gradational lower boundaries (exceptions are paleosols at 105 and 130 m depth which have gradational bottoms and tops with 20–30 cm thick horizons of maximum nodule concentration). Almost all paleosols observed in the field contained calcium carbonate nodules defining their Bk horizon. One prominent exception are the pair of Bk horizons at 279 m at the bottom of the section, which are developed in gravelly fluvial deposits and contain calcium carbonate root casts but no nodules. These two Bk horizons also had abrupt, planar upper and gradational lower boundaries. Some of the paleosols contained drab green and/or brown mottles and some paleosols had clay films coating ped surfaces (Fig. S1). Petrocalcic horizons, containing nodules up to 5 cm in diameter that are cemented together, were also observed in the section (Fig. S1), as were the cemented groundwater carbonate layers described by Heitmann et al. (2017). All calcium carbonate cemented layers were avoided for this work.

The accumulation of pedogenic calcium carbonate as the most prominent pedogenic feature leads us to classify these paleosols as Aridisols. The paleosols are certainly not Vertisols because they lack slickensides and wedge shaped peds. Neither are they Andisols because the parent material does not consist of volcanic ash. Some of the paleosols are demonstrably not Inceptisols because

they contain clay films coating ped surfaces and clay illuvation is minimal in Inceptisols. In addition, the well-developed calcic horizons in these paleosols are more typical for Aridisols than for Inceptisols. The paleosols could be Mollisols although there was no evidence for Mollic epipedons that would suggest classification as Mollisols, and the size of the roots in the lower part of the section indicate the presence of shrubs and not grasslands under which most Mollisols form. It is possible that the soils are Alfisols but the predominant pedogenic feature of accumulated calcium carbonate is more consistent with Aridisols.

Bulk paleosol samples containing carbonate nodules (or root casts in the case of the paleosols at 279 m at the bottom of the section) were sampled from >20 cm below paleosol tops (top of Bk horizons, making our 20 cm depth measurements conservative estimates of depth below paleosurface), although we also sampled across the entire Bk horizon of some paleosols. Paleosol carbonate samples were vacuum-impregnated with epoxy and made into polished thin sections. The thin sections were observed with a petrographic microscope to determine whether or not there were zones of spar to be avoided for stable isotope analysis. The carbonate nodules consist of dense micrite occluding matrix material and there is no evidence in the nodules analyzed for substantial secondary infilling with calcium carbonate precipitated from groundwater (Fig. 2). Even if there was a groundwater component in the nodules that was not apparent petrographically, its $\delta^{13}\text{C}$ values are probably very similar to those of the pedogenic carbonates, as suggested by comparison of pedogenic and groundwater carbonates from part of this section (Heitmann et al., 2017). The sediments in this section were shallowly buried (~280 m) and weakly lithified and therefore escaped intense burial diagenesis. Micritic carbonates were drilled from billets in preparation for stable isotope measurements. Samples for clumped isotope analysis were not impregnated with epoxy.

2.2. Geochemical analysis

2.2.1. Carbon isotope analysis

Stable carbon and oxygen isotope compositions of calcite were measured using a Thermo Electron Gasbench II coupled to a Thermo Electron 253 mass spectrometer in the stable isotope laboratory at the University of Texas at Austin. Results are reported relative to PDB defined by assigning NBS-19 calcite a $\delta^{13}\text{C}$ value of 1.95‰ and by assigning NBS-19 and NBS-18 $\delta^{18}\text{O}$ values of −2.2‰ and −23.2‰, respectively. The standard deviations for $\delta^{13}\text{C}$ and $\delta^{18}\text{O}$ measurements of calcite standards were $\pm 0.1\text{‰}$ and $\pm 0.2\text{‰}$, respectively.

To measure the carbon isotope composition of organic matter occluded inside the nodules, nodules were powdered and loaded into 5 mm × 9 mm silver capsules, loaded into a well plate, and then placed in a glass dessicator. The bottom of the dessicator had been previously filled with 6N hydrochloric acid (HCl) and no vacuum grease was used in the dessicator. The HCl vapor was allowed to react with samples for 1 day. This first step prevented vigorous reaction with liquid HCl treatments done next, which would otherwise overflow the silver capsules and result in loss of sample. After 1 day of reaction with HCl vapor, the well plate was removed from the dessicator and 1 drop of 6N HCl was added to each silver capsule. The well plate was then placed back into the dessicator overnight. The next day, the samples were moist but without standing liquid. 1 drop of 6N HCl was again added to each capsule following the same procedure, and this process of adding liquid HCl and then leaving the samples in the dessicator overnight was repeated until visible reaction with the liquid HCl ceased (typically 2–3 addition of liquid HCl). The insoluble residue was then dried and analyzed using an elemental analyzer coupled to a Delta V mass spectrometer in the stable isotope laboratory at the Univer-

sity of Texas at Austin. The measured $\delta^{13}\text{C}$ values were normalized to the PDB scale using the slope of a 3-point calibration curve constructed from measurements of international standards IAEA C5, IAEA C7 and USGS 24 over the course of several days during runs in which the unknowns were also analyzed. A single slope was used for all unknowns. The intercept of the calibration curve varied among runs and was determined for each run by assigning IAEA C5 (the standard with the most similar $\delta^{13}\text{C}$ values to the unknowns) a $\delta^{13}\text{C}$ value of −25.5‰. Within run reproducibility of replicate measurements of IAEA C5 was better than $\pm 0.2\text{‰}$ (1σ , $n = 5$ per run).

2.2.2. Clumped isotope analyses

Carbonate clumped isotope thermometry utilizes the thermodynamically-driven increase in the concentration of ^{13}C – ^{18}O bonds in the carbonate crystal lattice with decreasing temperature to determine the temperature of carbonate formation (Ghosh et al., 2006). The abundance of “clumped” ^{13}C – ^{18}O bonds in a carbonate sample, relative to the abundance that would be expected for the random distribution of isotopes, is measured with high-precision mass spectrometry and quantified as the Δ_{47} parameter (where 47 refers to mass-47 analyte CO_2 gas, which is mostly the clumped species $^{13}\text{C}^{18}\text{O}^{16}\text{O}$, produced from phosphoric acid digestion of the carbonate sample). For this study, clumped isotope analyses of micritic carbonates were carried out at the University of Washington IsoLab. Sample preparation for clumped isotope analysis followed the methods of Burgener et al. (2016). In brief, carbonate samples (6–8 mg) were digested for 10 minutes in a common bath of phosphoric acid (specific gravity 1.9–1.95) held at 90 °C. To separate out water, the liberated CO_2 gas was cryogenically purified through a sequence of ethanol-dry ice (~−80 °C) and liquid nitrogen traps. For removal of hydro/halocarbon and sulfur-compound contaminants, the CO_2 was subsequently entrained in He and passed through a Porapak Q column (50/80 mesh, 15 cm long, 4.5 mm ID, 0.635 mm OD) held between −10 °C and −20 °C. Purified CO_2 was then analyzed on a dual-inlet Thermo MAT 253 with 6 mm tubing, standard MEMCO Faraday cup configuration and built-in, automated 10-port tube cracker inlet system. To start each sample analysis, sample bellows were fully expanded and evacuated. Sample gas was then filled into the sample bellows and pressure was measured. Following sample gas filling, evacuated reference bellows at 100% expansion were filled to a pressure equal to that measured in the sample bellows with UW ‘fermented corn’ reference CO_2 ($\delta^{13}\text{C}_{\text{PDB}} = -10.2\text{‰}$, $\delta^{18}\text{O}_{\text{VSMOW}} = -6.0\text{‰}$; values calibrated by NBS-19 international carbonate standard). Masses 44–46 were measured with standard amplification (3×10^8 , 3×10^{10} , 1×10^{11} , respectively); masses 47–49 were measured with 1×10^{12} Ω amplification. At the end of each 6-acquisition sample measurement, water backgrounds were measured by peak centering on the mass-45 Faraday collector and measuring m/z 18 of both sample and reference. C and O stable isotopic values were referenced to international standards: NBS-19 and LSVEC for $\delta^{13}\text{C}$, and to NBS-18 and NBS-19 for $\delta^{18}\text{O}$. Δ_{47} based soil temperature results were calculated based on the synthetic carbonate calibration of Kelson et al. (2017).

2.3. Paleosol carbonate CO_2 barometer

Paleoatmospheric CO_2 concentrations reported here were determined following Cerling (1999):

$$[\text{CO}_2]_{\text{atm}} = S(z) \left[\frac{\delta^{13}\text{C}_c - (1.0044\delta^{13}\text{C}_r + 4.4)}{\delta^{13}\text{C}_a - \delta^{13}\text{C}_c} \right] \quad (1)$$

where $S(z)$ is the soil-derived component of total CO_2 in the soil (i.e. $S(z) = [\text{CO}_2]_{\text{soil}} - [\text{CO}_2]_{\text{atm}}$) at depth z , $\delta^{13}\text{C}$ is the carbon isotope composition in standard delta notation; s , r and a refer to soil

CO₂, soil-respired CO₂ and atmospheric CO₂, respectively; and the coefficient 1.0044 and the constant 4.4 derive from the difference in diffusivity between ¹³CO₂ and ¹²CO₂. Based on the classification of these paleosols as Aridisols, the distribution of *S*(*z*) values in modern Aridisols was used for the newly reported record in this paper. The *S*(*z*) distribution for modern Aridisols is quite wide, with a median value of 440 ppm and 16th and 84th percentile values of 240 and 1075 ppm, respectively; the full distribution, modified from Montañez (2013) (*n* = 35) is given in the computer program PBUQ (Breecker, 2013). $\delta^{13}\text{C}$ is the carbon isotope composition in standard delta notation; *s*, *r* and *a* refer to soil CO₂, soil-respired CO₂ and atmospheric CO₂, respectively; and the coefficient 1.0044 and the constant 4.4 derive from the difference in diffusivity between ¹³CO₂ and ¹²CO₂. The value of $\delta^{13}\text{C}_s$ is calculated from measured $\delta^{13}\text{C}$ values of soil carbonate and the soil carbonate formation temperatures following Romanek et al. (1992):

$$\varepsilon_{\text{calcite-CO}_2} = 1000 \left(\frac{1000 + \delta_{\text{calcite}}}{1000 + \delta_{\text{CO}_2}} - 1 \right) = 11.98 - 12T$$

where *T* has units of °C. The temperatures used here were determined by clumped isotope thermometry (see section 2.2.). In this paper we used the $\delta^{13}\text{C}_a$ values calculated from contemporaneous $\delta^{13}\text{C}$ values of benthic foraminifera by Tipple et al. (2010).

The $\delta^{13}\text{C}$ values of organic matter in soils typically increase with depth. Soil respiration rates also typically decrease with depth, such that A horizon organic matter is probably more representative of the $\delta^{13}\text{C}$ value of soil respiration than B horizon organic matter, even though soil carbonates used for paleoatmospheric CO₂ reconstruction typically occur in soil B horizons. Unfortunately, in the rock record, soil A horizons are frequently either eroded or overprinted by B horizons during aggradations. Furthermore, organic matter occluded inside paleosol carbonates (in the paleosol B horizons) is arguably better preserved than organic matter not protected by carbonates (although this needs further study). Thus, we use B horizon organic matter (occluded in carbonate nodules) to determine the $\delta^{13}\text{C}$ value of respired CO₂. Breecker (2013) suggested subtraction of 1‰ from B horizon organic matter to represent the $\delta^{13}\text{C}$ value of respired CO₂ (which is dominantly from the A horizon).

2.4. Previously published Miocene CO₂ records

Miocene atmospheric CO₂ concentrations have been reconstructed using numerous proxies including $\delta^{11}\text{B}$ values of foraminifera (e.g., Foster et al., 2012; Badger et al., 2013; Greenop et al., 2014), the carbon isotope fractionation during algal growth as recorded by alkenones (e.g., Badger et al., 2013; Zhang et al., 2013b), foraminiferal B/Ca ratios (Tripathi et al., 2009), paleosol carbonates (e.g., Breecker, 2013; Breecker and Retallack, 2014; Heitmann et al., 2017) and the stomata of fossil plant leaves (Van Der Burgh et al., 1993; Royer et al., 2001a; Kürschner et al., 2008; Beerling et al., 2009; Retallack, 2009; Stults et al., 2011; Wang et al., 2015). In our multiproxy analysis, we consider the $\delta^{11}\text{B}$, stomatal and paleosol carbonate records. We do not include paleosol-based estimates for which paleosol organic matter was not measured because $\delta^{13}\text{C}$ values of terrestrial organic matter can be highly spatially and temporally variable and unreliably determined from $\delta^{13}\text{C}$ values of atmospheric CO₂ (Breecker and Retallack, 2014). We also avoided all alkenone records due to unquantified uncertainty associated with cell size/geometry and active carbon uptake (e.g. Bolton and Stoll, 2013). A few recent studies have attempted to account for cell size, growth rate and active carbon uptake (e.g. Mejía et al., 2017) and we plot their CO₂ concentrations, but there are not a sufficient number of such data points during the Miocene Climate Optimum to consider this proxy in our

uncertainty analysis. We also avoid the B/Ca record because recent work suggests that B/Ca in rapidly precipitated carbonates is more sensitive to growth rate than to pH (Uchikawa et al., 2015).

2.5. Uncertainty quantification and data analysis

For the uncertainty associated with CO₂ determinations from proxies other than paleosols, see supplementary methods. To quantify error associated with paleosol-based CO₂ determinations, we used the computer program PBUQ (Breecker, 2013) to propagate error through Equation (1). Briefly, PBUQ uses a Monte Carlo approach with 10,000 iterations to propagate error associated with the input values in Equation (1) that result from both analytical error and calibration error. For every determination, the program outputs 10,000 realizations of atmospheric CO₂ which define a distribution useful for probabilistic analysis. PBUQ has multiple user-selected options for the determination of each input value. For this work, we used the following selections: 1) Δ_{47} for carbonate formation temperature, 2) *S*(*z*) based on soil order, 3) organic matter (OM) occluded in paleosol carbonate for the $\delta^{13}\text{C}_r$, 4) Tipple et al. (2010) for $\delta^{13}\text{C}_a$.

In order to address the basic question of whether or not there was a MCO-wide peak in CO₂, we defined time periods among which we compared CO₂. The MCO time period extended from 17.4–14 Ma based on the midpoints of benthic $\delta^{18}\text{O}$ ramps (Mudelsee et al., 2014). The time periods preceding and following the MCO were both assigned a duration of 3 Myr (pre-MCO: 20.4–17.4 Ma and post-MCO: 14–11 Ma, respectively), long enough to incorporate a substantial number of CO₂ estimates and short enough to encompass rather small benthic $\delta^{18}\text{O}$ changes. CO₂ proxies likely reconstruct CO₂ change more accurately than absolute CO₂ and thus are more comparable among proxies. We therefore calculated the factor CO₂ change from post MCO values. Time series of the factor CO₂ change were smoothed using local polynomial regression fitting (LOESS), with the optimal smoothing parameter determined by leave-one-out cross validation. We also plotted PDFs (probability density functions) and CDFs (cumulative distribution functions) of the factor CO₂ change ratio among time periods (i.e., MCO/pre-MCO, MCO/post-MCO, pre-MCO/post-MCO) in order to quantitatively evaluate the occurrence of a CO₂ peak during the MCO (see supplementary material for detailed methods).

We also compared the within-time period variance of both CO₂ and benthic $\delta^{18}\text{O}$ values among the pre-MCO, MCO and post-MCO. For CO₂, we used the medians of individual determinations. For benthic $\delta^{18}\text{O}$ values we used the records from sites 1146 and 1237 (Holbourn et al., 2005), site 1171 (Shevenell et al., 2004), site 1090 (Billups et al., 2002) and site 926 (Shackleton and Hall, 1997; Pälike et al., 2006). The ages of the beginning and ending of the MCO were defined individually for each $\delta^{18}\text{O}$ record following Mudelsee et al. (2014). When comparing the $\delta^{18}\text{O}$ variance among pre-MCO, MCO and post-MCO, we considered subsets of each record such that there was an equal duration of $\delta^{18}\text{O}$ data within each of the time periods being compared. We used the F-test, Levene test and Brown–Forsythe tests of equal variance.

3. Results

The $\delta^{13}\text{C}$ values of carbonate nodules ($\delta^{13}\text{C}_c$) and occluded organic matter ($\delta^{13}\text{C}_{\text{om}}$) were higher during the MCO (17.4 to 14 Myr) than post MCO (14 to 11 Myr) (Figs. 3C, 3D). Values of $\delta^{13}\text{C}_c$ varied from −4.2‰ to −9.1‰ (*n* = 19); the average value of $\delta^{13}\text{C}_c$ decreased from $-5.3 \pm 0.3\text{‰}$ (*n* = 8) during the MCO to $-6.2 \pm 0.7\text{‰}$ (*n* = 6) during the post MCO and $-7.3 \pm 0.3\text{‰}$ (*n* = 5) during the late Miocene, respectively. Values of $\delta^{13}\text{C}_{\text{om}}$ varied from −23.5‰ to −26.1‰ (*n* = 19). The average value of $\delta^{13}\text{C}_{\text{om}}$

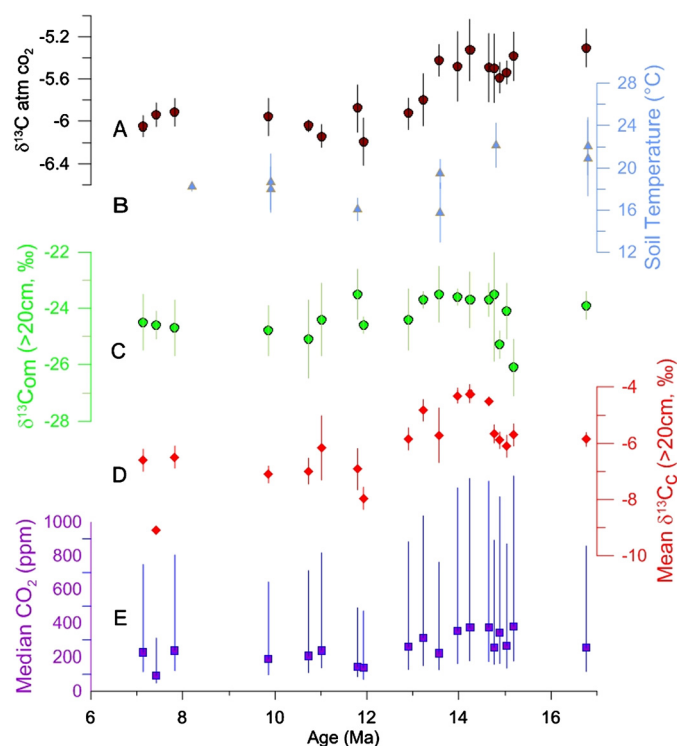


Fig. 3. Middle to late Miocene $p\text{CO}_2$ reconstruction and the changes in relevant parameters A) $\delta^{13}\text{C}$ values of atmospheric CO_2 (Tippie et al., 2010), B) Δ_{47} temperature record, C) $\delta^{13}\text{C}$ values of organic matter occluded in carbonate, D) $\delta^{13}\text{C}$ values of carbonate nodules (mean value of nodules >20 below the paleosurface), E) reconstructed $p\text{CO}_2$ records. Values of B, C and D are needed to calculate the CO_2 concentration using equation (1) (see methods).

decreased from $-24.2 \pm 0.9\text{‰}$ ($n = 8$) during the MCO to $-24.0 \pm 0.8\text{‰}$ ($n = 6$) during the post MCO and $-24.7 \pm 0.9\text{‰}$ ($n = 5$) during the late Miocene, respectively.

The measured carbonate clumped isotope (Δ_{47}) values varied from 0.617 to 0.649 ‰ ($n = 10$; Tables S1 and S2). Δ_{47} based soil temperature $T(\Delta_{47})$ varied from 22 to $13 \pm 2^\circ\text{C}$. During the MCO, mean soil temperature was $22 \pm 3^\circ\text{C}$ ($n = 3$), which decreased to a mean value of $17 \pm 2^\circ\text{C}$ ($n = 3$) during the post MCO and $17 \pm 3^\circ\text{C}$ ($n = 4$) during the late Miocene, respectively (Fig. 3B). We interpolated using a first-order polynomial between the 10 temperature determinations to estimate carbonate formation temperature at each stratigraphic level where $\delta^{13}\text{C}$ measurements were made. The clumped isotope temperatures are substantially lower than the temperature ($25 \pm 10^\circ\text{C}$) used by Heitmann et al. (2017).

The $\delta^{13}\text{C}$ values of organic matter occluded in nodules is higher than the $\delta^{13}\text{C}$ values of organic matter (-27.1‰) reported by Heitmann et al. (2017) from part of this same section (within Unit 1 corresponding to 13.5–13.4 Ma). Heitmann et al. (2017) measured the $\delta^{13}\text{C}$ values of organic matter occluded in bulk paleosol material and used a different pretreatment/decarbonation method than used here. To determine whether the observed difference was due to pretreatment or to a real difference between sample types, we analyzed the different samples types (bulk paleosol and nodules) with the same pretreatment technique (see supplementary material for more details). The $\delta^{13}\text{C}$ value of the organic matter in the nodules was 1–4 ‰ higher than the $\delta^{13}\text{C}$ value of organic matter occluded in bulk paleosol material, even when the same pretreatment method was used. We conclude that the organic matter inside the nodules has $\delta^{13}\text{C}$ values higher than the organic matter occluded in carbonates in the bulk paleosols material, and that the former are the most representative of soil respired CO_2 during nodule formation. We therefore use the $\delta^{13}\text{C}$

values of organic matter occluded in the nodules to make the CO_2 determinations reported here.

Heitmann et al. (2017) used a $\delta^{13}\text{C}$ value of organic matter of -27.1‰ and temperature of $25 \pm 10^\circ\text{C}$ for the part of the section for which we use a $\delta^{13}\text{C}_{\text{om}}$ value of -23.6‰ and temperature of $17.5 \pm 3^\circ\text{C}$. Our best estimate reported here for this part of the section is 220 ppm. Using the Heitmann et al. (2017) $\delta^{13}\text{C}_{\text{om}}$ value results in 390 ppm and using both Heitmann $\delta^{13}\text{C}_{\text{om}}$ and Heitmann assumed T , results in 475 ppm.

For our new record reported here, medians of CO_2 distributions calculated using equation (1) (Table S3) are higher during the MCO (250–400 ppm) than later in the Miocene (100–300 ppm) (Fig. 3E). The CO_2 concentrations at the end of the MCO are among the highest in our record and coincide with high benthic $\delta^{13}\text{C}$ values (Fig. 3). The 10,000 realizations for each determination are provided in the supplementary material. When considered alongside other paleosol-based CO_2 determinations compiled by Breecker and Retallack (2014) based on previously reported data (Table S3), the median CO_2 concentrations define a distinct peak during the MCO (Fig. 4A, B). The LOESS smoothed curve that considers CO_2 determined by all three proxies also shows elevated MCO CO_2 values and shows that the MCO CO_2 peak was symmetrical (Fig. 4C), in contrast to benthic $\delta^{18}\text{O}$ change across this interval which was distinctly asymmetrical, with lower $\delta^{18}\text{O}$ values during the pre-MCO than post-MCO (Fig. 4D). Using all proxies, we estimate an average CO_2 level during the MCO of $375+150/-100$ (84th and 16th percentile) ppm with a 40% probability of $\text{CO}_2 > 400$ ppm, 20% probability of $\text{CO}_2 > 500$ ppm, 10% probability of $\text{CO}_2 > 600$ ppm and 2% probability of $\text{CO}_2 > 800$ ppm (Fig. 5, see supplementary material for a description of the averaging method).

Calculating the factor CO_2 change from the mean post-MCO CO_2 level brings into agreement the results of stomata- and paleosol-based records, especially during the pre-MCO time period, suggesting there was little variability in CO_2 before the onset of the MCO (Fig. 4B). Elevated MCO CO_2 is indicated independently by boron isotopes, stomata and paleosols. Considering together all the factor CO_2 changes calculated by proxy, our calculations indicate >80% and >70% probability of elevated MCO CO_2 compared with the immediately following and preceding intervals, respectively, and that the most probable magnitude of the MCO CO_2 peak is 12.5% higher than pre-MCO and 20% higher than post-MCO levels (Fig. 6). Larger factors of perhaps 50% higher CO_2 likely apply in narrower time slices of <1 Myr (Fig. 4). CO_2 during the pre- and post-MCO time periods were similar to each other within the precision of the existing determinations, with a slight (60%) probability of higher means of proxy-based CO_2 medians during the pre-MCO than post-MCO (Fig. 6).

The variance in median CO_2 is significantly larger during the MCO than during both the pre-MCO and the post-MCO (all tests significant at the $\alpha = 0.05$ level) time periods. The variance is higher for the MCO even if the beginning of the MCO is defined as 16.6 Ma to group the low CO_2 values from 16.6–17.4 (Fig. 4) with the pre-MCO rather than MCO (i.e. the low CO_2 values at the beginning of the MCO are not the cause of the elevated MCO variance in CO_2). The variance in median CO_2 was also probably larger during the post-MCO than pre-MCO (F-test and Levene test significant, Brown–Forsythe test $p = 0.08$). In addition, the effect of varying the age of time period boundaries by ± 0.2 Myr does not substantially change the comparisons of means or variances among the time periods (Fig. S2).

The variance of benthic foraminifera $\delta^{18}\text{O}$ values is also significantly larger during the MCO than during both the post-MCO (for sites 761, 1146, 1237 and 1171, all the tests were all significant at the $\alpha = 0.05$ level) and pre-MCO (for site 1090, all three test were significant). This analysis indicates that benthic $\delta^{18}\text{O}$ variance was larger during the MCO than it was before or after the MCO. In

addition, benthic $\delta^{18}\text{O}$ variance was significantly larger during the pre-MCO than during the post-MCO at site 926 (F test is not significant but Levene test and Brown–Forsythe test are significant; the discrepancy between test results occurred because a substantial portion of the variance in the post-MCO benthic $\delta^{18}\text{O}$ data at site 926 is controlled by a single high $\delta^{18}\text{O}$ value, resulting in a non-normal distribution and thus violating a basic assumption of the F test).

4. Discussion

4.1. Absolute CO_2 during the MCO

The average MCO atmospheric CO_2 concentration determined from three independent proxies is substantially lower than the concentrations required by models to reproduce MCO warmth. A CO_2 level of 800 ppm (Goldner et al., 2014) is at the extreme upper limit (98th percentile) of our estimates (Fig. 5). A higher climate sensitivity during MCO may in part explain this model-data mismatch. Nonetheless our CO_2 record and the analysis of the CO_2 compilation described here emphasizes the difficulty in modeling MCO warmth, as previously discussed in detail (Goldner et al., 2014).

A caveat to the proxy-based average CO_2 in addition to those regarding averaging methods (see supplementary material) is that while there is now decent coverage during the MCO, the CO_2 records are still rather low resolution and we do not know for certain whether or not the proxy-based CO_2 determinations are biased toward certain orbital configurations and/or glacial or interglacial states, nor do we know whether such a bias would be problematic because we have not quantified the magnitude of CO_2 variability at the orbital scale for the Miocene. A final caveat is that the proxies, especially when applied in deep time, are probably much better at resolving CO_2 change (discussed below) than absolute CO_2 , although it is possible that averaging among proxies reduces such errors (if some proxies are biased high and others low). The similarity among proxies suggest that these biases, if they exist, are relatively small but it remains possible that all three proxies are biased in the same direction. Additional independent proxies would help in this regard.

4.2. Climate and CO_2 change across the middle Miocene

During the latter part of the MCO (15–14 Ma) benthic $\delta^{18}\text{O}$ values increased slightly but were nonetheless near the minimum values of the Neogene (e.g., Holbourn et al., 2007; Zachos et al., 2008). The paleosols in the Yanwan section record elevated CO_2 at this time, with factor changes in CO_2 from post-MCO that are similar to the mean factor change recorded by other proxies during the thermal maximum earlier in the MCO (Fig. 4). We suggest that modestly elevated mean CO_2 supported continued warmth during

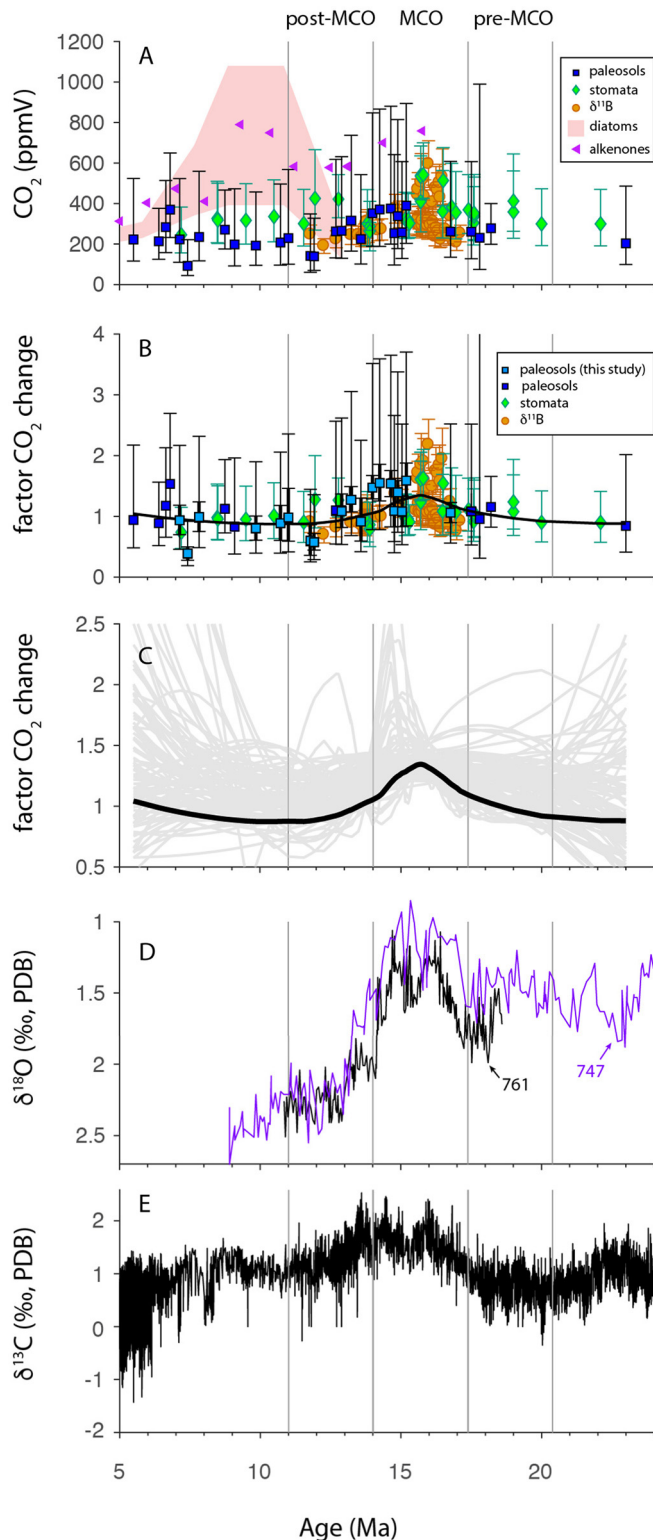


Fig. 4. Miocene CO_2 and benthic $\delta^{18}\text{O}$ records. A) Proxy-based CO_2 records during the Miocene. Data compiled from literature: foraminifera $\delta^{11}\text{B}$ (Foster et al., 2012; Badger et al., 2013; Greenop et al., 2014), stomata (Van Der Burgh et al., 1993; Royer et al., 2001b; Kürschner et al., 2008; Beerling et al., 2009; Retallack, 2009; Stults et al., 2011; Wang et al., 2015) and paleosols (see Table S3 for detail). The red field is defined by maximum and minimum CO_2 determined from carbon isotope fractionation during photosynthesis in pennate diatoms (Mejía et al., 2017). The purple triangles are from carbon isotope fractionation during photosynthesis in Haptophyte algae (using alkenones) from records of Pagani et al. (2005), Seki et al. (2010), Zhang et al. (2013b), Bolton et al. (2016). Carbon concentration mechanisms were accounted for in both the diatom and alkenones records using the ACTI-CO model (Mejía et al., 2017). B) The factor change in CO_2 from the mean of post-MCO medians. The smaller magnitude error bars on the paleosol-based factor CO_2 changes assume all paleosols have the same $S(z)$ value whereas the larger magnitude error bars assume independent $S(z)$. The most accurate representation of uncertainty lies between these two error bars (see supplementary material). C) LOESS smoothed factor CO_2 change considering all three proxies. We randomly sampled one value from each factor CO_2 change distribution and smoothed the resulting CO_2 versus time curve. We generated 100 such smoothed curves (gray lines). For each curve, new random values were selected from each distribution and a new optimal smoothing parameter was chosen by leave-one-out cross validation. Heavy black line shows LOESS smoothing of the medians of each CO_2 determination. The smoothed curve is intended to show changes in CO_2 on the million-year timescale. D) Benthic $\delta^{18}\text{O}$ records from ODP site 761 (Holbourn et al., 2004) and ODP site 747 (Wright and Miller, 1992). E) Global benthic $\delta^{13}\text{C}$ stack (Zachos et al., 2008). Vertical gray lines represent the boundaries of time periods.

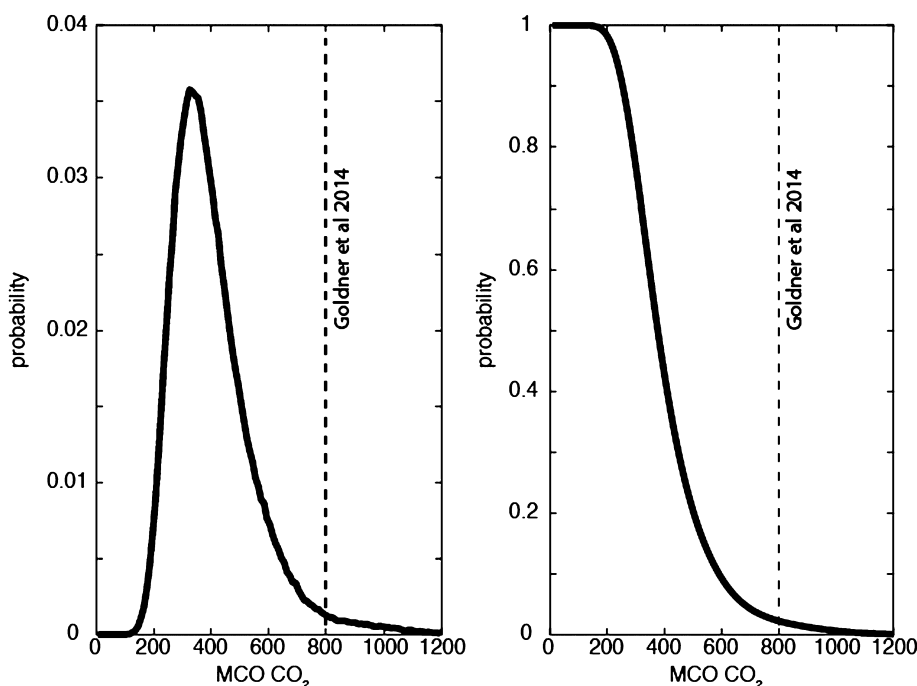


Fig. 5. Estimates based on three proxies of average MCO atmospheric CO₂. The PDF (left) and CDF (right) were generated by first averaging among individual determinations by proxy and then averaging among the proxies. See supplementary material for a more detailed description of how these curves were calculated. The minimum CO₂ concentration required by the most recent climate modeling to match MCO warmth is shown as the dashed line (Goldner et al., 2014).

this latter part of the MCO. Our new CO₂ record also provides further support for the argument against organic carbon burial and CO₂ drawdown as the driver of the Monterey excursion, which spans the interval over which we reconstruct elevated CO₂ (e.g., Vincent and Burger, 1985; Zachos et al., 2008, Fig. 3).

The Yanwan section paleosols record CO₂ decrease across the MCT coincident with abrupt increase in $\delta^{18}\text{O}$ values of benthic foraminifera (Wright and Miller, 1992; Holbourn et al., 2005, 2007) and seawater (Lear et al., 2015) and a final peak in benthic $\delta^{13}\text{C}$ values (Zachos et al., 2008; Holbourn et al., 2005). Thus our CO₂ record supports previous interpretations that MCT cooling and Antarctic ice sheet expansion was associated with organic carbon burial and a decrease in CO₂ (Kürschner et al., 2008; Foster et al., 2012; Badger et al., 2013; Holbourn et al., 2014). That interpretation is now supported independently by three different CO₂ proxies (paleosols, stomata and foraminiferal $\delta^{11}\text{B}$) (Fig. 4).

Our analysis indicates that not only was mean MCO CO₂ elevated, but that the variance in CO₂ was also elevated compared to the immediately preceding (20.4–17.4 Ma) and following (14–11 Ma) time periods. This observation is consistent with the high CO₂ variance during the earlier part of the MCO reported previously (Greenop et al., 2014). Relatively large variability and modestly elevated mean CO₂ during the MCO coincided with relatively large variability in benthic $\delta^{18}\text{O}$ values. The $\delta^{18}\text{O}$ value of seawater was also highly variable during the MCO (Lear et al., 2015). These observations are consistent with a reduced stability of the Antarctic ice sheets during the MCO because CO₂ was elevated and/or variable. Such ice sheet variability with CO₂ in the range of 280 to 500 ppm is now reproduced by models (Gasson et al., 2016). The difference in variability between the pre-MCO and post-MCO is also relevant to climate-CO₂ relationships during the middle Miocene. Benthic $\delta^{18}\text{O}$ values were more variable during the pre-MCO than post-MCO, yet mean CO₂ was similar and the CO₂ variability was probably larger during the latter when $\delta^{18}\text{O}$ variability was smaller. These considerations suggest that neither mean CO₂ nor the magnitude of CO₂ variability explain the relative stability of the Antarctic ice sheets after the MCT.

Importantly, the lowest CO₂ levels indicated by individual proxy-based determinations during the MCO are quite similar to the CO₂ levels during the pre- and post-MCO time periods. For each proxy (paleosols, stomata and $\delta^{11}\text{B}$) the lowest CO₂ during the MCO is indistinguishable within error from the lowest CO₂ during the post-MCO (after the MCT) (Fig. 4A). However, the highest benthic $\delta^{18}\text{O}$ values during the MCO were similar to or lower than the lowest benthic $\delta^{18}\text{O}$ values after the MCT (Holbourn et al., 2007, 2014). This observation suggests that the decrease in CO₂ across the MCT, although perhaps necessary, was not sufficient for ice sheet expansion unless either 1) ice volume was so sensitive to CO₂ during the middle Miocene that CO₂ differences smaller than proxies are currently able to resolve explain ice volume increase across the MCT or 2) the low CO₂ episodes during the MCO were too short to drive ice sheet expansion to the extent that occurred across the MCT. The existing records show that pre-MCO CO₂ was not substantially higher than post-MCO CO₂ despite the observation that benthic $\delta^{18}\text{O}$ values were substantially lower during the pre-MCO than post-MCO (by about 0.6‰, Mudelsee et al., 2014). Considering the mean of proxy-based CO₂ medians, the existing CO₂ records suggest only 60% probability that CO₂ concentrations were higher during the pre-MCO than post-MCO and only about 30% probability that CO₂ concentrations were >25% higher during the pre-MCO than post-MCO (Fig. 6). Furthermore, the existing CO₂ records, although low resolution, suggest that the variability of CO₂ during the pre-MCO was small, suggesting that even sustained CO₂ at near post-MCO levels was not sufficient to drive the magnitude of ice sheet expansion observed during the MCT. This leaves high sensitivity of ice volume to CO₂ or the importance of another factor as the remaining explanations for MCT ice sheet expansion.

4.3. Drivers of the MCT

MCT ice sheet expansion has been previously related to two factors other than CO₂: orbitally-controlled low seasonality over Antarctica allowing snow cover to persist through summer (Hol-

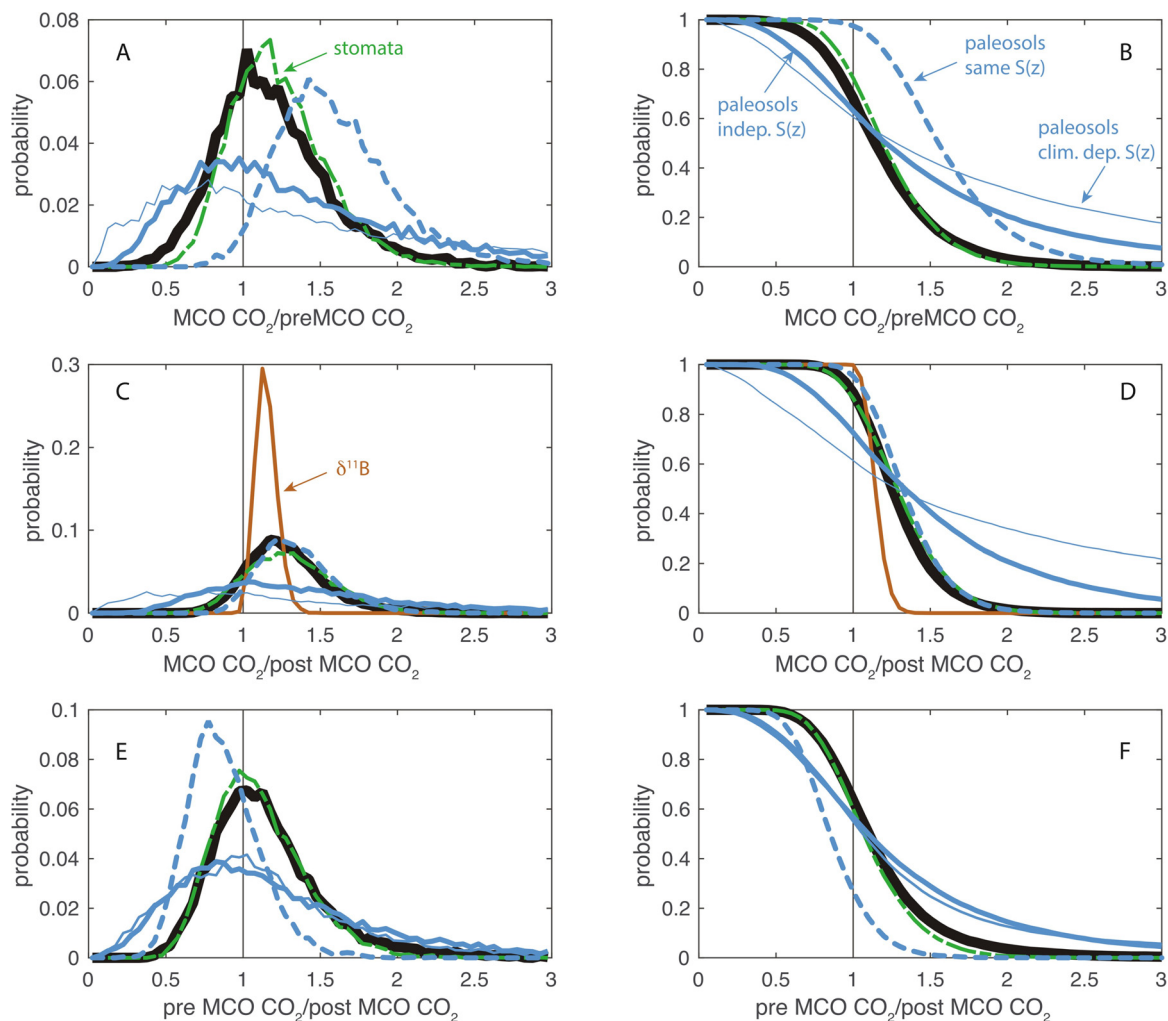


Fig. 6. Probabilities of Miocene CO₂ change. The PDFs (A, C, E) and CDFs (B, D, F) show the probabilities (y axis) of the factor change in CO₂ between various time periods (x axis). The black curves are a best estimate calculated using all proxies together. The orange curves were calculated using the foraminifera δ¹¹B records and the green lines using the stomatal records. Results from paleosols are shown in blue and assume that $S(z)$ values are 1) independent among paleosols (heavy blue line), 2) the same among all paleosols (dashed blue line) and 3) dependent on climate (i.e. $S(z)$ values are the same among paleosols within each time period but not necessarily the same between paleosols in different time periods, thin blue line). The best estimate of the uncertainty is somewhere between the independent and same $S(z)$ scenarios (heavy and dashed blue lines). The climate-dependent $S(z)$ scenario represents a conservatively large uncertainty. See supplementary material for a detailed description of the three $S(z)$ scenarios and the methods used to generate this plot.

bourne et al., 2005, 2007) and tectonic closure of the eastern Tethys, shutting off warm, saline deep water production and thus slowing meridional heat transport, cooling the Southern Ocean and strengthening the Antarctic Circumpolar Current (e.g., Woodruff and Savin, 1989; Flower and Kennett, 1994; Shevenell et al., 2004; Hamon et al., 2013). The orbitally-controlled low seasonality over Antarctica may also have been necessary, but not sufficient given that similar orbital configuration also occurred during the pre-MCO (recurrence every ~2.4 Myr). Neither was the coincidence of low CO₂ (i.e. post-MCO levels) and low seasonality sufficient to drive MCT ice sheet expansion as these conditions also occurred during the pre-MCO. We therefore suggest that cooling of the Southern Ocean due to closure of the eastern Tethys (Hamon et al., 2013) prior to ice sheet expansion (Shevenell et al., 2004) pushed the climate system across a threshold such that orbitally-controlled low seasonality in Antarctica (Holbourn et al., 2005) initiated carbon cycle-climate feedbacks such as enhanced equatorial upwelling with high latitude cooling (Badger et al., 2013; Holbourn et al., 2014) that were strong enough to drive ice sheet expansion during the MCT. Previous modeling concluded that Tethys closure and resulting ACC strengthening was not sufficient to drive MCT cooling (Hamon et al., 2013). Our results provide a

different, but consistent perspective, that Tethys closure and ACC strengthening were necessary for MCT cooling, even if they were not the proximal trigger. The symmetry of CO₂ change and asymmetry of climate change across the MCO indicates that there was a shift in the sensitivity of Earth's climate to CO₂ sometime during the MCO. With few temperature estimates, especially from the pre-MCO time period, and still rather large error associated with average MCO CO₂, it is difficult to quantify the magnitude of this change in sensitivity. However, if we assume that the ratio of global MAT changes (MCO-post-MCO)/(pre-MCO-MCO) is approximated by the ratio of the respective benthic δ¹⁸O shifts across these boundaries (0.9‰/0.3‰ = 3, Mudelsee et al., 2014) then the similar CO₂ during pre-MCO and post-MCO time periods suggests that climate sensitivity increased from pre-MCO to post-MCO by a factor of 3. Some component of the relatively low benthic δ¹⁸O values during the pre-MCO is perhaps attributable to low latitude (Tethyan) deep water formation which would have resulted in higher bottom water temperatures compared with solely high latitude deep water formation, but Tethyan waters probably also had higher δ¹⁸O values than their high latitude counterparts, to some degree negating the effect of higher temperatures on benthic foraminifera δ¹⁸O values. Increases of up to 0.8‰ in South Pacific

(site 591b) benthic $\delta^{18}\text{O}$ values during the MCO have been interpreted to record shifts from Tethyan to high latitude deep water formation (Flower and Kennett, 1995). If the location of deep water formation had such large effects globally, then the asymmetry of benthic $\delta^{18}\text{O}$ values on either side of the MCO could be entirely explained by a shift from dominant Tethyan to dominant high latitude deep water formation rather than a difference in ice volume and high latitude temperature. However, simulations using the fully coupled climate model FOAMv1.5 suggest a climate sensitivity approximately $3\times$ larger for Miocene boundary conditions, including an open and deep Tethys sea, than for modern day (Hamon et al., 2013), supporting the idea that Tethys closure had a profound effect on climate sensitivity. A fully coupled climate model (CCSM3) forced with Miocene boundary conditions, including an open and deep Tethys sea, and year 1990's CO_2 does not simulate much warming (1.5°C compared to modern control, Herold et al., 2012) suggesting that an open and deep Tethys explains only a portion of the relative warmth of the Miocene. Thus, Tethys closure may explain the asymmetry of climate change across the MCO, but it is apparently insufficient to explain the difference between MCO and modern climate.

The paleosol and stomatal records show no substantial change in CO_2 during the Miocene after about 12 Ma, in contrast to a recent diatom-based CO_2 record (Mejía et al., 2017). The global benthic $\delta^{18}\text{O}$ stack shows only slight $\delta^{18}\text{O}$ increase during this period. Our CO_2 records show slightly larger variations during 8–6 Ma, when the alkenone unsaturation parameter data shows a phase of global surface ocean cooling (Herbert et al., 2016). At this point, our CO_2 records have too few datapoints to test whether CO_2 and ocean surface temperature are coupled during this period. More CO_2 records are required to investigate CO_2 -climate relationships during the late Miocene.

4.4. Conclusions

There was a modest peak in atmospheric CO_2 concentrations during the MCO. The variability of CO_2 during the MCO was large and the lowest CO_2 during the MCO was similar within uncertainty to the CO_2 levels before and after the MCO. Atmospheric CO_2 concentrations decreased during the MCT reaching values similar to those before the MCO. Therefore, neither the CO_2 decrease, the orbital-controlled low seasonality over Antarctica, nor their co-occurrence was sufficient to drive MCT ice sheet expansion. Rather, closure of the Tethys and associated changes in ocean circulation were necessary first steps that increased the sensitivity of Earth's climate to atmospheric CO_2 .

Acknowledgements

Thanks to D. Royer for help compiling CO_2 determinations and for help with error propagation for stomatal-based determinations. This work is co-supported by the National Key Research and Development Program of China (grant No. 2016YFE0109500), the National Natural Science Foundation of China (Grant Nos. 41761144063; 41672157; 41422204), the Fundamental Research Funds for the Central Universities (Grant Nos. lzujbky-2018-ot05; lzujbky-2014-257; lzujbky-2016-sp05), the open fund from State Key Laboratory of Loess and Quaternary Geology, Institute of Earth Environment, CAS (SKLLQG1608), the State Scholarship Fund organized by the China Scholarship Council (CSC) in 2014 (grant No. 201406180052) and National Science Foundation of the United States of America (PIRE grant 1545859; EAR-1156134; EAR-1252064).

Appendix A. Supplementary material

Supplementary material related to this article can be found online at <https://doi.org/10.1016/j.epsl.2018.07.011>.

References

- Badger, M.P., Lear, C.H., Pancost, R.D., Foster, G.L., Bailey, T.R., Leng, M.J., Abels, H.A., 2013. CO_2 drawdown following the middle Miocene expansion of the Antarctic Ice Sheet. *Paleoceanography* 28 (1), 42–53.
- Bereiter, B., Eggelston, S., Schmitt, J., Nehrbass-Ahles, C., Stocker, T.F., Fischer, H., Kipfstuhl, S., Chappellaz, J., 2015. Revision of the EPICA Dome C CO_2 record from 800 to 600 kyr before present. *Geophys. Res. Lett.* 42 (2), 542–549.
- Beerling, D.J., Fox, A., Anderson, C., 2009. Quantitative uncertainty analysis of ancient atmospheric CO_2 estimates from fossil leaves. *Am. J. Sci.* 309 (9), 775–787.
- Billups, K., Channell, J., Zachos, J., 2002. Late Oligocene to early Miocene geochronology and paleoceanography from the subantarctic South Atlantic. *Paleoceanography* 17.
- Breecker, D.O., 2013. Quantifying and understanding the uncertainty of atmospheric CO_2 concentrations determined from calcic paleosols. *Geochem. Geophys. Geosyst.* 14 (8), 3210–3220.
- Breecker, D.O., Retallack, G.J., 2014. Refining the pedogenic carbonate atmospheric CO_2 proxy and application to Miocene CO_2 . *Palaeogeogr. Palaeoclimatol. Palaeoecol.* 406, 1–8.
- Bolton, C.T., Stoll, H.M., 2013. Late Miocene threshold response of marine algae to carbon dioxide limitation. *Nature* 500 (7464), 558–562.
- Bolton, C.T., Hernández-Sánchez, M.T., Fuertes, M.A., González-Lemos, S., Abrevaya, L., Mendez-Vicente, A., Flores, J.A., Probert, I., Giosan, L., Johnson, J., Stoll, H.M., 2016. Decrease in coccolithophore calcification and CO_2 since the middle Miocene. *Nat. Commun.* 7, 10284.
- Burgener, L., Huntington, K.W., Hoke, G.D., Schauer, A., Ringham, M.C., Latorre, C., Díaz, F.P., 2016. Variations in soil carbonate formation and seasonal bias over >4 km of relief in the western Andes (30°S) revealed by clumped isotope thermometry. *Earth Planet. Sci. Lett.* 441, 188–199.
- Cerling, T.E., 1999. Stable carbon isotopes in paleosol carbonates. *Palaeoweathering, palaeosurfaces and related continental deposits. Spec. Publ. Int. Assoc. Sedimentol.* 27, 43–60.
- Glugokenky, E., Tans, P., 2016. Trends in atmospheric carbon dioxide. Available at www.esrl.noaa.gov/gmd/ccgg/trends/.
- Foster, G.L., Lear, C.H., Rae, J.W.B., 2012. The evolution of $p\text{CO}_2$, ice volume and climate during the middle Miocene. *Earth Planet. Sci. Lett.* 341–344, 243–254.
- Flower, B.P., Kennett, J.P., 1993. Middle Miocene ocean–climate transition: high-resolution oxygen and carbon isotopic records from Deep Sea Drilling Project Site 588A, southwest Pacific. *Paleoceanography* 8 (6), 811–843.
- Flower, B.P., Kennett, J.P., 1994. The middle Miocene climatic transition: east Antarctic ice sheet development, deep ocean circulation and global carbon cycling. *Palaeogeogr. Palaeoclimatol. Palaeoecol.* 108 (3–4), 537–555.
- Flower, B.P., Kennett, J.P., 1995. Middle Miocene deepwater paleoceanography in the Southwest Pacific: relations with East Antarctic ice-sheet development. *Paleoceanography* 10 (6), 1095–1112.
- Gasson, E., Deconto, R.M., Pollard, D., Levy, R.H., 2016. Dynamic Antarctic ice sheet during the early to mid-Miocene. *Proc. Natl. Acad. Sci. USA* 113 (13), 3459–3464.
- Goldner, A., Herold, N., Huber, M., 2014. The challenge of simulating the warmth of the mid-Miocene climate optimum in CESM1. *Clim. Past* 10, 523–536.
- Greenop, R., Foster, G.L., Wilson, P.A., Lear, C.H., 2014. Middle Miocene climate instability associated with high-amplitude CO_2 variability. *Paleoceanography* 29 (9), 845–853.
- Ghosh, P., Adkins, J., Affek, H., Balta, B., Guo, W., Schauble, E.A., Schrag, D., Eiler, J.M., 2006. ^{13}C – ^{18}O bonds in carbonate minerals: a new kind of paleothermometer. *Geochim. Cosmochim. Acta* 70, 1439–1456.
- Hamon, N., Sepulchre, P., Lefebvre, V., Ramstein, G., 2013. The role of East-Tethys seaway closure in the middle Miocene climatic transition (ca. 14 Ma). *Clim. Past* 9 (6), 2687–2702.
- Herbert, T.D., Lawrence, K.T., Tzanova, A., Peterson, L.C., Caballero-Gill, R., Kelly, C.S., 2016. Late Miocene global cooling and the rise of modern ecosystems. *Nat. Geosci.* 9 (11), 843–847.
- Herold, N., Huber, M., Muller, R.D., Seton, M., 2012. Modeling the Miocene climatic optimum: ocean circulation. *Paleoceanography* 27, PA1209. <https://doi.org/10.1029/2010PA002041>.
- Heitmann, E.O., Ji, S.H., Nie, J.S., Breecker, D.O., 2017. Orbitally-paced variations of water availability in the SE Asian Monsoon region following the Miocene Climate Transition. *Earth Planet. Sci. Lett.* 474.
- Holbourn, A., Kuhnt, W., Simo, J.T., Li, Q., 2004. Middle Miocene isotope stratigraphy and paleoceanographic evolution of the northwest and southwest Australian margins (Wombat Plateau and Great Australian Bight). *Palaeogeogr. Palaeoclimatol. Palaeoecol.* 208, 1–22.
- Holbourn, A.E., Kuhnt, W., Schulz, M., Erlenkeuser, H., 2005. Impacts of orbital forcing and atmospheric carbon dioxide on Miocene ice-sheet expansion. *Nature* 438 (7067), 483–487.
- Holbourn, A.E., Kuhnt, W., Schulz, M., Flores, J.A., Andersen, N., 2007. Orbitally-paced climate evolution during the middle Miocene “Monterey” carbon-isotope excursion. *Earth Planet. Sci. Lett.* 261 (3), 534–550.
- Holbourn, A.E., Kuhnt, W., Lyle, M.W., Schneider, L.J., Romero, O.E., Andersen, N., 2014. Middle Miocene climate cooling linked to intensification of eastern equatorial Pacific upwelling. *Geology* 42 (1), 19–22.

- Kelson, J.R., Huntington, K.W., Schauer, A.J., Saenger, C., Lechler, A.R., 2017. Toward a universal carbonate clumped isotope calibration: diverse synthesis and preparatory methods suggest a single temperature relationship. *Geochim. Cosmochim. Acta* 197, 104–131. <http://doi.org/10.1016/j.gca.2016.10.010>.
- Kürschner, W.M., Kvacek, Z., Dilcher, D.L., 2008. The impact of Miocene atmospheric carbon dioxide fluctuations on climate and the evolution of terrestrial ecosystems. *Proc. Natl. Acad. Sci.* 105, 449–453.
- Lear, C.H., Coxall, H.K., Foster, G.L., Lunt, D.J., Mawbey, E.M., Rosenthal, Y., Sosdian, S.M., Thomas, E., Wilson, P.A., 2015. Neogene ice volume and ocean temperatures: insights from infaunal foraminiferal Mg/Ca paleothermometry. *Paleoceanography* 30, 1437–1454. <https://doi.org/10.1002/2015PA002833>.
- McKay, D.I.A., Tyrrell, T., Wilson, P.A., Foster, G.L., 2014. Estimating the impact of the cryptic degassing of Large Igneous Provinces: a mid-Miocene case-study. *Earth Planet. Sci. Lett.* 403, 254–262.
- Meinshausen, M., Smith, S.J., Calvin, K., Daniel, J.S., Kainuma, M.L., Lamarque, J.F., Matsumoto, K., Montzka, S.A., Raper, S.C., Riahi, K., Thomson, A., Velders, G.J., Vuuren, D.P., 2011. The RCP greenhouse gas concentrations and their extensions from 1765 to 2300. *Clim. Change* 109 (1–2), 213–241.
- Mejía, L.M., Méndez-Vicente, A., Abrevaya, L., Lawrence, K.T., Ladlow, C., Bolton, C., Cacho, I., Stoll, H., 2017. A diatom record of CO₂ decline since the late Miocene. *Earth Planet. Sci. Lett.* 479, 18–33.
- Miller, K.G., Fairbanks, R.G., Mountain, G.S., 1987. Tertiary oxygen isotope synthesis, sea level history, and continental margin erosion. *Paleoceanography* 2 (1), 1–19.
- Montañez, I.P., 2013. Modern soil system constraints on reconstructing deep-time atmospheric CO₂. *Geochim. Cosmochim. Acta* 101, 57–75.
- Mudelsee, M., Bickert, T., Lear, C.H., Lohmann, G., 2014. Cenozoic climate changes: a review based on time series analysis of marine benthic $\delta^{18}\text{O}$ records. *Rev. Geophys.* 52. <https://doi.org/10.1002/2013RG000440>.
- Pagani, M., Authur, M.A., Freeman, K.H., 1999. Miocene evolution of atmospheric carbon dioxide. *Paleoceanography* 14, 273–292.
- Pagani, M., Zachos, J.C., Freeman, K.H., Tipler, B., Bohaty, S., 2005. Marked decline in atmospheric carbon dioxide concentrations during the Paleogene. *Science* 309, 600–603.
- Pälike, H., Frazier, J., Zachos, J.C., 2006. Extended orbitally forced palaeoclimatic records from the equatorial Atlantic Ceara Rise. *Quat. Sci. Rev.* 25, 3138–3149.
- Retallack, G.J., 1988. Field recognition of paleosols. *Spec. Pap., Geol. Soc. Am.* 216, 1–20.
- Retallack, G.J., 2009. Greenhouse crises of the past 300 million years. *Geol. Soc. Am. Bull.* 121, 1441–1455.
- Romanek, C.S., Grossman, E.L., Morse, J.W., 1992. Carbon isotopic fractionation in synthetic aragonite and calcite: effects of temperature and precipitation rate. *Geochim. Cosmochim. Acta* 56 (1), 419–430.
- Royer, D.L., Berner, R.A., Beerling, D.J., 2001a. Phanerozoic atmospheric CO₂ change: evaluating geochemical and palaeobiological approaches. *Earth-Sci. Rev.* 54, 349–392. [https://doi.org/10.1016/S0012-8252\(00\)00042-8](https://doi.org/10.1016/S0012-8252(00)00042-8).
- Royer, D.L., Wing, S.L., Beerling, D.J., Jolley, D.W., Koch, P.L., Hickey, L.J., Berner, R.A., 2001b. Palaeobotanical evidence for near present-day levels of atmospheric CO₂ during part of the Tertiary. *Science* 292, 2310–2313.
- Seki, O., Foster, G.L., Schmidt, D.N., Mackensen, A., Kawamura, K., Pancost, R.D., 2010. Alkenone and boron-based Pliocene pCO₂ records. *Earth Planet. Sci. Lett.* 292, 201–211.
- Shackleton, N., Hall, M., 1997. The late Miocene stable isotope record, Site 926. In: *Proc. Ocean Drill. Program Sci. Results*, vol. 154, pp. 367–373.
- Shevenell, A.E., Kennett, J.P., Lea, D.W., 2004. Middle Miocene Southern Ocean cooling and Antarctic cryosphere expansion. *Science* 305 (5691), 1766–1770.
- Stults, D.Z., Wagner-Cremer, F., Axsmith, B.J., 2011. Atmospheric paleo-CO₂ estimates based on Taxodium distichum (Cupressaceae) fossils from the Miocene and Pliocene of Eastern North America. *Palaeogeogr. Palaeoclimatol. Palaeoecol.* 309 (3), 327–332.
- Tripathi, A.K., Roberts, C.D., Eagle, R.A., 2009. Coupling of CO₂ and ice sheet stability over major climate transitions of the last 20 million years. *Science* 326 (5958), 1394–1397.
- Tipple, B.J., Meyers, S.R., Mark, P., 2010. Carbon isotope ratio of Cenozoic CO₂: a comparative evaluation of available geochemical proxies. *Paleoceanography* 25 (3), 375–387. <https://doi.org/10.1029/PA001851>.
- Uchikawa, J., Penman, D.E., Zachos, J.C., Zeebe, R.E., 2015. Experimental evidence for kinetic effects on B/Ca in synthetic calcite: implications for potential B(OH)₄⁻ and B(OH)₃ incorporation. *Geochim. Cosmochim. Acta* 150, 171–191.
- Van Der Burgh, J., Visscher, H., Dilcher, D.L., Kürschner, W.M., 1993. Paleoatmospheric signatures in Neogene fossil leaves. *Science* 260, 1788–1790.
- Vincent, E., Burger, W.H., 1985. Carbon dioxide and polar cooling in the Miocene: the Monterey hypothesis. In: Sundquist, E.T., Broecker, W.S. (Eds.), *The Carbon Cycle and Atmospheric CO₂: Natural Variations Archean to Present*, vol. 32. AGU, Washington D.C., pp. 455–468.
- Woodruff, F., Savin, S.M., 1989. Miocene deepwater oceanography. *Paleoceanography* 4 (1), 87–140.
- Wright, J., Miller, K., 1992. Miocene stable isotope stratigraphy, Site 747, Kerguelen Plateau. In: Wise, S.W., et al. (Eds.), *In: Proc. Ocean Drill. Program Sci. Results*, vol. 120, pp. 855–866.
- Wang, Y.Q., Momohara, A., Wang, L., Lebreton-Anberrée, J., Zhou, Z.K., 2015. Evolutionary history of atmospheric CO₂ during the late Cenozoic from fossilized *Metasequoia* needles. *PLoS ONE* 10(7), e0130941.
- Zachos, J.C., Dickens, G.R., Zeebe, R.E., 2008. An early Cenozoic perspective on greenhouse warming and carbon-cycle dynamics. *Nature* 451 (7176), 279–283.
- Zhang, J., Li, J.J., Song, C.H., Zhao, Z., Xie, G., Wang, X., Hui, Z.C., Peng, T.J., 2013a. Palaeomagnetic ages of Miocene fluvio-lacustrine sediments in the Tianshui Basin, western China. *J. Asian Earth Sci.* 62, 341–348.
- Zhang, Y.G., Pagani, M., Liu, Z.H., Bohaty, S.M., DeConto, R., 2013b. A 40-million-year history of atmospheric CO₂. *Philos. Trans. R. Soc. A* 371, 20130096.